

Coarsening dynamics of topological defects in thin Permalloy films

Ilari Rissanen* and Lasse Laurson

*COMP Centre of Excellence and Helsinki Institute of Physics,
Department of Applied Physics, Aalto University,
P.O.Box 11100, FI-00076 Aalto, Espoo, Finland.*

We study the dynamics of topological defects in the magnetic texture of rectangular Permalloy thin film elements during relaxation from random magnetization initial states. Our full micromagnetic simulations reveal complex defect dynamics during relaxation towards the stable Landau closure domain pattern, manifested as temporal power-law decay, with a system-size dependent cut-off time, of various quantities. These include the energy density of the system, and the number densities of the different kinds of topological defects present in the system. The related power-law exponents assume non-trivial values, and are found to be different for the different defect types. The exponents are robust against a moderate increase in the Gilbert damping constant and introduction of quenched structural disorder. We discuss details of the processes allowed by conservation of the winding number of the defects, underlying their complex coarsening dynamics.

PACS numbers: 75.78.-n, 76.60.Es, 75.70.Kw

I. INTRODUCTION

The topic of coarsening dynamics of topological defects in diverse systems ranging from liquid crystals^{1–4} to biosystems⁵ and cosmology⁶ has attracted considerable interest as it is related to properties of symmetry-breaking phase transitions. As the system is quenched from a high-temperature disordered phase to a low-temperature ordered phase, the symmetry of the disordered phase is broken and topological defects are generated, subsequently exhibiting slow coarsening dynamics⁷. Such phase-ordering kinetics is often characterized by a power-law temporal decay $\rho(t) \sim t^{-\eta}$ of the density ρ of the defects, with the value of the exponent η depending on the characteristics of the system, and/or the defects⁸.

In ferromagnetic thin films dominated by shape anisotropy, elementary topological defects within the magnetic texture, i.e. vortices, antivortices and edge defects, may occur^{9–11}. For instance, magnetic domain walls can be envisaged as composite objects consisting of two or more such elementary defects, each characterized by their integer or fractional winding numbers⁹. Also, the presence of vortices is intimately related to magnetic flux closure patterns minimizing the stray field energy of micron or submicron magnetic particles^{12–14}. While coarsening of e.g. the domain structures in Ising and Potts type of models^{15,16} as well as that of the defect structure in the XY model^{1,17} have been extensively studied, less is known about the details of coarsening dynamics in soft (low-anisotropy) ferromagnetic thin films, involving the collective dynamics of vortices, antivortices and edge defects, when all the relevant effective field terms (exchange, and demagnetizing energies) are included in the description.

Here we study, by performing an extensive set of full micromagnetic simulations of the magnetization dynamics in Permalloy thin films, the relaxation process of such magnetic topological defects, starting from random magnetization initial states, mimicking the high-

temperature disordered paramagnetic phase. Our zero-temperature simulations, resembling a rapid quench to the low-temperature ferromagnetic phase, show how defects emerge from the disordered initial states, and subsequently exhibit coarsening dynamics. The focus of our study is on the time period after a short initial transient such that the length of the magnetization vectors is approximately constant, and the system can be modeled by the Landau-Lifshitz-Gilbert equation. In the coarsening process, the densities of the various defect types, as well as the energy density of the system¹⁸, follow power-law temporal decay towards the ground state with a flux-closure Landau pattern. These power laws are characterized by non-trivial exponent values which are different for the different defect types, and exhibit a cut-off time scale growing with the system size. We also address the question of how the values of these exponents are affected by changes in the Gilbert damping constant α and introduction of random structural disorder within the film, and discuss the role of the conservation of the winding number on the possible annihilation reactions, underlying the complex coarsening dynamics of the various defect populations.

The paper is organized as follows: In the following section (Section II), properties of the elementary topological defects in soft ferromagnetic thin films are reviewed, and details of the micromagnetic simulations and data analysis are presented in Section III. In Section IV, we show our results on the defect coarsening dynamics and analyze the possible annihilation reactions underlying such dynamics. Finally, Section V finishes the paper with discussion and conclusions.

II. TOPOLOGICAL DEFECTS IN MAGNETICALLY SOFT THIN FILMS

In the absence of an external magnetic field, the orientation of the spins in thin films of magnetically soft

material such as Permalloy is determined by the competition of shape anisotropy and exchange interaction. For small films or nanodots (up to few tens of nanometers depending on the film/dot thickness¹⁹), the exchange interaction energy dominates and the ground state is a single magnetic domain²⁰. In larger films, up to a couple of tens of microns²¹, the ground state configuration consists of one or more elementary topological defects, depending on the geometry of the film⁹. Square thin films can contain three types of stable elementary magnetic defects: vortices, antivortices and edge defects. Other structures, such as domain walls, are composed of these elementary defects.

Magnetic vortex is a point defect with core radius approximately equal to the magnetic exchange length of the material (between 5 and 6 nm in Permalloy²²). The core magnetization, often referred to as the polarization of the vortex, points out of the thin film plane, while the surrounding magnetization rotates around the core (Fig. 1 a). Vortices are thus characterized by two quantities: the core polarization, and the rotation direction of the surrounding magnetization (clockwise or counter-clockwise).

An antivortex is another type of point defect with out-of-plane polarization, with a core radius similar to that of vortices. Unlike vortices, however, the magnetization around an antivortex does not rotate around the core of the defect. Instead, the magnetization points into the core from two opposite directions and out of the core from two perpendicular directions, with the rest of the surrounding magnetization assuming orientation in between these main directions (Fig. 1 b)¹⁰.

Vortices and antivortices are both bulk defects, i.e. they form in the bulk of the film and tend to stay away from the edges unless driven there by the relaxation or an outside influence such as an external magnetic field. The third type of defects, edge defects, are confined to the edge and cannot move to the bulk⁹. The edge defects are also different from vortices and antivortices in that the core magnetization of the defect does not necessarily point out of plane. Edge defects can further be divided into two types, henceforth referred to as the positive edge defect (Fig. 1 c) and negative edge defect (Fig. 1 d), according to their winding numbers.

The topological defects can be characterized by the winding number W , defined as a normalized line integral of the magnetization vector angle θ over a closed loop around the defect¹⁰, $W = \frac{1}{2\pi} \oint_S \theta(\phi) ds$, where ϕ is the angle of the vector from the defect core to the point on the line being integrated over, and S the integration path. The winding number (or topological charge) is $+1$ for vortices and -1 for antivortices. Though edge defects cannot be similarly circled around, they can be shown to have fractional winding numbers of $\pm 1/2$.⁹

The total winding number of a thin film is a conserved quantity. In a film with n holes, the total winding number is $W = \sum_{i=1}^k W_i = 1 - n$, where W_i is the winding number of defect i and k is the number of defects⁹. The

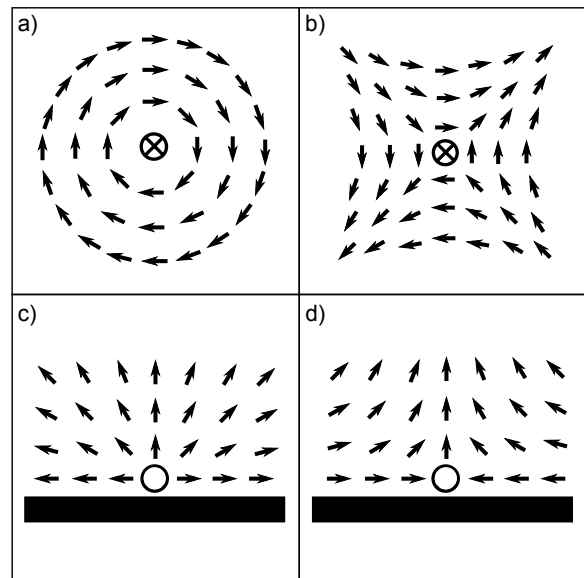


Figure 1. The elementary topological defects: **a)** vortex, **b)** antivortex, **c)** positive edge defect, **d)** negative edge defect. The film is viewed from the direction of the z -axis, with the arrows showing the magnetization direction in the xy -plane. The vortex/antivortex cores pointing out of plane are denoted with \otimes . In the case of edge defects, the cores (not necessarily out of plane) are marked with \circ and the black bar represents the edge of the sample.

total number of defects can be quite high in large magnetically unrelaxed films, but the number will eventually decay due to the collision-induced annihilations of the defects. In a film with no holes, such as the ones simulated in this paper, the total winding number is equal to 1. This corresponds to a few possible configurations, out of which the single vortex state (*flux-closure* or *Landau pattern*) is energetically most favorable¹³.

III. MICROMAGNETIC SIMULATIONS

A. Simulation details

During the relaxation of the magnetization from a randomized initial state, the time evolution of the magnetic moments $\mathbf{m} = \mathbf{M}/M_s$ is described by the Landau-Lifshitz-Gilbert (LLG) equation,

$$\frac{\partial \mathbf{m}}{\partial t} = \gamma \mathbf{H}_{\text{eff}} \times \mathbf{m} + \alpha \mathbf{m} \times \frac{\partial \mathbf{m}}{\partial t}, \quad (1)$$

where γ is the gyromagnetic ratio, \mathbf{H}_{eff} the effective magnetic field, M_s the saturation magnetization, and α the Gilbert damping constant. \mathbf{H}_{eff} takes into account four energy contributions, which are the aforementioned exchange energy, energy due to magnetocrystalline anisotropy, Zeeman energy (energy of an external field) and the demagnetizing field energy. In the context of this work, the Zeeman and anisotropy contribu-

tions are negligible, as no external fields are being applied and the magnetocrystalline anisotropy of Permalloy is insignificant.

Simulations were performed with a GPU-based micro-magnetic code Mumax3, using the adaptive Dormand-Prince method and finite differences for temporal and spatial discretization, respectively²³. Simulations were run for square samples of thickness 20 nm, with four different linear film sizes L of 512 nm, 1024 nm, 2048 nm and 4096 nm. The dimensions of a single simulation cell were chosen to be $4 \text{ nm} \times 4 \text{ nm} \times 20 \text{ nm}$, so that the smallest film corresponds to 128×128 cells; the number of out-of-plane z -direction cells is 1. Here, typical parameter values of Permalloy^{13,18,24} are used, i.e., $M_s = 860 \cdot 10^3 \text{ A/m}$, and $A = 13 \cdot 10^{-12} \text{ J/m}$. Unless stated otherwise, we consider $\alpha = 0.02$, which corresponds to slightly Nd-doped²⁵ or Pt-doped²⁶ Permalloy. We also investigate the effect of α on the relaxation process, using values ranging from the typical 0.01 for pure Permalloy up to 0.1 representing highly doped Permalloy, and a couple of very high values, $\alpha = 0.5$ and $\alpha = 0.9$. While the latter two α -values are clearly too high to realistically describe magnetization dynamics of Permalloy, they allow to address the more general question of the effect of damping on the defect coarsening dynamics. Moreover, we also check the stability of our results with respect to adding quenched structural disorder to the system^{27–31}, by performing a Voronoi tessellation to divide the films into grains, mimicking the polycrystalline structure of the material^{30,31}; we consider average grain sizes of 10 nm, 20 nm and 40 nm. Disorder is then implemented by either setting a random saturation magnetization in each grain (from a normal distribution with mean M_s and standard deviation of $0.1M_s$ or $0.2M_s$)^{27,30}, or decreasing the exchange coupling across the grain boundaries by 10 %, 30 % or 50 %^{30,31}.

At the start of the simulation, the magnetization is randomized in each cell, after which the system is let relax at zero temperature without external magnetic fields. Four example snapshots of the relaxation process are shown in Fig. 2. The relaxation process consists of approximately three phases. In the beginning of the relaxation (usually from 0 to approx. 1 ns, though less with stronger damping), the system experiences large fluctuations in magnetization without well-defined magnetic defects or domains. After these fluctuations have settled, the dynamics consist of defects moving and annihilating with each other; the properties of this defect coarsening dynamics are the main focus of the paper. The final relaxation stage consists of a single vortex experiencing damped gyrational motion towards the center of the film. The configuration of the resulting ground state displays the Landau pattern: four large domains separated by diagonal domain walls starting from the corners of the film and meeting at a 90° angle in a vortex at the center^{12–14}.

One should note that during the very early stages of the relaxation starting from the disordered paramagnetic state, the LLG equation does not fully describe the mag-

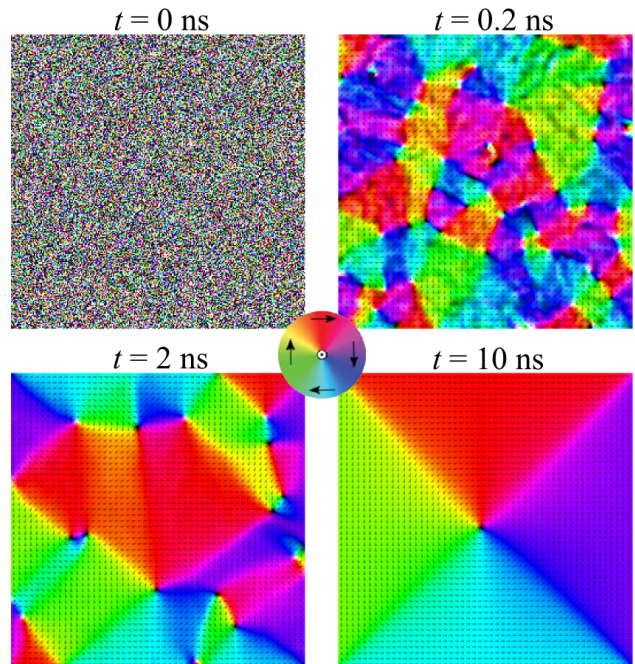


Figure 2. The relaxation process in a square thin film with lateral size $L = 1024 \text{ nm}$. The color wheel in the center shows the direction of the magnetization corresponding to each color. In this case, the final vortex (black dot at the center of the bottom right picture) is a $-z$ -polarized clockwise vortex.

netization dynamics since it assumes that the lengths of the magnetic moments are conserved; the latter is not strictly speaking the case during the first stage of quenching the system across the phase boundary from the high-temperature paramagnetic to the ferromagnetic phase. However, multiple studies^{32–34} concerning the longitudinal relaxation of the magnetic moments point out that in low temperatures, the longitudinal relaxation is orders of magnitude faster than the transverse relaxation, and takes place in the femto- and picosecond timescale. Thus, after the first few picoseconds, and especially in the annihilation-dominated relaxation regime which is the focus of the present study, longitudinal relaxation is nonexistent, and the LLG equation suffices to fully describe the magnetization dynamics.

B. Locating and characterizing defects

Here, we describe the algorithm used to find the defects from the magnetization data. Finding bulk defects (vortices and antivortices) is relatively simple, as they have strong z -directional magnetization at the core. The cores of the defects are determined by comparing the z -magnetization with the nearest neighbors and finding the local maximum or minimum, and comparing it to a threshold value of $0.5M_s$. The type of the defect is then determined by performing a discretized version

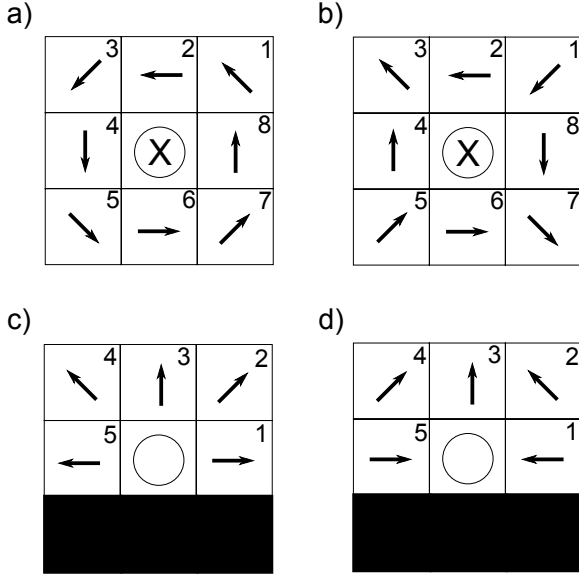


Figure 3. A schematic view of the different defects and the (ideal) surrounding magnetization in the nearest neighbors in the xy -plane, similarly as in Fig. 1. The numbers in the corners of the cells show the cell traversal order when determining the defect type.

of the winding number integration: The nearest neighbors are looped through in a circle, and the rotation direction of the magnetization vector is monitored. Doing a counterclockwise loop, the vector in two consecutive cells would turn left in the case of a vortex and right in the case of an antivortex (Fig. 3 a,b). Ideally, the angle between two consecutive neighbors in the xy -plane would be 45° . Since each magnetization vector is normalized to M_s , the length of the cross product of two consecutive magnetization vectors in the vortex case (choosing counterclockwise turn as positive) would yield $||\mathbf{m}_i \times \mathbf{m}_{i+1}|| = M_s^2 \sin 45^\circ = \frac{M_s^2}{\sqrt{2}}$. The corresponding result for an antivortex would be $-M_s^2/\sqrt{2}$. Summing the results for each neighbor pair, this method would ideally give $2\sqrt{2}M_s^2$ for vortices and $-2\sqrt{2}M_s^2$ for antivortices. Due to nonidealities in rotation and the fact that the spins in the cells neighboring the core also tend to have nonzero z -components, the sums can be smaller. Thus, threshold values for recognizing defects are set to M_s^2 and $-M_s^2$ for vortices and antivortices, respectively.

In addition to the winding number, the vortices can have clockwise or counterclockwise rotation. The rotation is determined as above, but considering the center-to-neighbor vector and the magnetization vector for each neighbor. This approach would ideally yield $4M_s(1+\sqrt{2})$ for counterclockwise rotation and $-4M_s(1+\sqrt{2})$ for clockwise rotation, since the angle between the vectors would be 90° . Due to nonidealities, threshold values were set to $5M_s$ and $-5M_s$, respectively.

Edge defects are somewhat harder to detect, as they usually do not have polarized cores. Thus the defects are

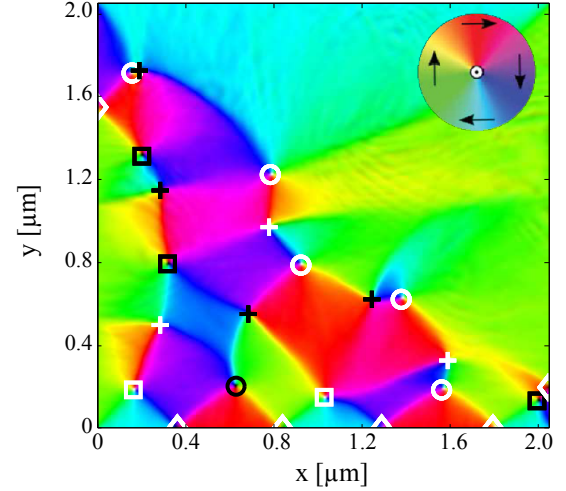


Figure 4. The various kinds elementary defects present in the relaxation of the largest film: clockwise vortices (squares), counterclockwise vortices (circles), antivortices (+-signs) and edge defects (triangles). The color of a bulk defect shows its polarization (black for $-z$ and white for $+z$). For the edge defects, the color indicates whether the winding number of the defect is positive (black) or negative (white).

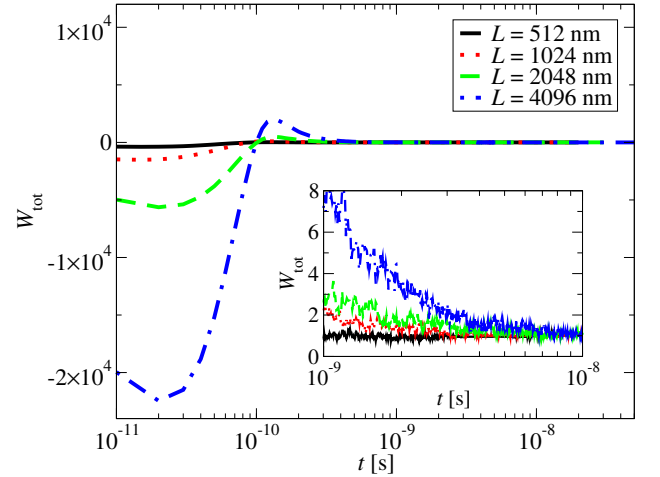


Figure 5. The total average winding numbers for the four film sizes used. The inset shows that the winding number for the largest sizes takes more time to converge into 1.

determined only by performing a loop through the nearest neighbors as in the case of bulk defects (Fig. 3 c,d). Though the method performed quite well in finding the edge defects, the difficulty of singling out the core sometimes resulted in multiple detections in the same region. This problem was somewhat mitigated by introducing an area around the edge defects in which similar defects would be ignored. Fig. 4 shows a snapshot of the relaxation with defects pinpointed by the detection algorithm.

In the simulations, the initial random fluctuations cause many false defect detections. This can be seen as the total winding number fluctuating in the beginning

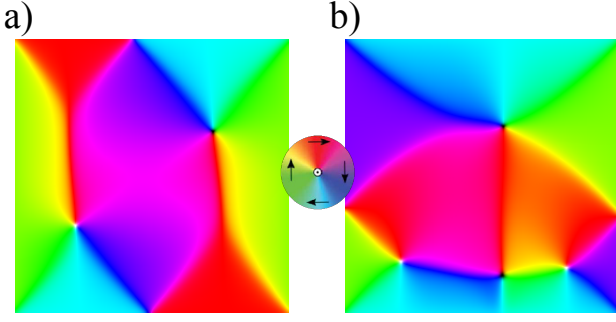


Figure 6. The two most commonly encountered metastable states, shown for the system with $L = 1024$ nm. **a)** A two edge defect, two vortex state which also displays significant bending of domain walls. **b)** A more complex state, showing an isolated vortex and an arc of other defects.

before converging close to 1 (Fig. 5). The tendency of the total winding number to be below 0 in the beginning is due to the initial fluctuations being more easily categorized as antivortices, since they do not have a rotation direction threshold. The winding number can also change momentarily during annihilations due to the detection algorithm having difficulties determining defects that are very close to one another. Moreover, sometimes a disturbance (such as a spin wave from an annihilation) near a defect could cause the defect to become momentarily unrecognizable to the algorithm. To lessen the fluctuation in defect amounts, a persistence time of 20 ps for the already detected defects was introduced. During the persistence time, the algorithm considers a defect to exist in the location it was last detected even if it can't find it at the present time. The persistence time reduces the noise in the number of defects.

IV. RESULTS

Depending on the system size, the relaxation from random magnetization to the single vortex ground state took usually approximately from 5 ns to 40 ns. Hence the simulations were run for 20 ns for the two smallest film sizes, 30 ns for the $L = 2048$ nm film and 50 ns for the largest film. Usually the ground state was reached relatively quickly compared to the simulation time. Only with the largest film size there were a couple of instances in which the system had not relaxed to the single-vortex state or a metastable state before the simulation time ran out, though in these cases the system was still close to the relaxed state with only 2 – 4 defects left.

Metastable states were encountered in 10 of the total 80 simulations. With the smallest film, only one simulation ended up in a metastable state, whereas each larger size had three simulations finished in a metastable state. Of these states, two different kinds were common: a simple one with two negative edge defects on two opposite sides and two vortices close to the center (Fig. 6 a) and a

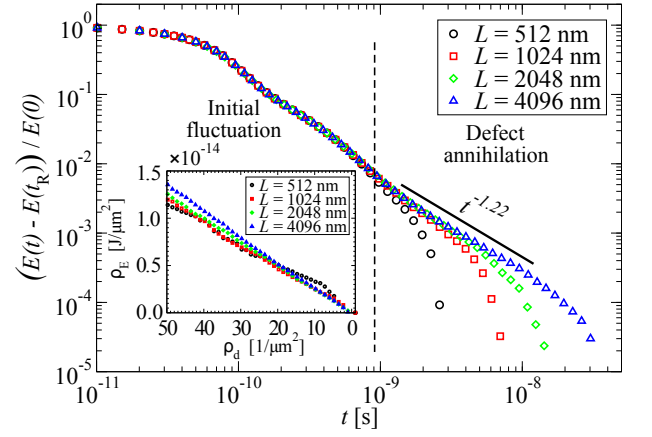


Figure 7. The time evolution of the total energy of the films, consisting of an “initial fluctuation” phase independent of the system size, and a defect annihilation/coarsening phase displaying power law relaxation terminated by a cut-off time increasing with the film size. The linear dependence of energy density and defect density during the coarsening phase is shown in the inset.

more complicated state with an antivortex, three vortices and two edge defects (Fig. 6 b), in which one vortex is isolated and the other defects are in an arc close to one of the edges.

A. Time evolution of energy and defect densities

In Fig. 7, the time evolution of the energy towards the value $E(t_R)$ is shown for all four system sizes, averaged over 20 simulations for each size. Here t_R is the time after which the number of defects in the system does not decrease, which corresponds to either the single vortex state, a metastable state with more than one defect, or the state the system had time to reach before the simulation time ran out.

The total energy of the system drops very little in the first 0.1 ns, and then starts decreasing in a slightly oscillating fashion in the initial fluctuation regime (0 – 1 ns). Stable defects start to form at roughly 0.5 ns, but the energy evolution is dominated by the global fluctuations in the system. As can be seen from the figure, during the initial phase the time evolution of the energy, normalized by the initial value, is independent of the system size. This results from the fact that during the initial fluctuations the magnetization is largely random, and thus the energy contributions from the exchange interaction and the stray fields are proportional to the system size.

In the “defect annihilation” or coarsening phase, the time evolution of the energy resembles a power law $E(t) - E(t_R) \propto t^{-\eta_E}$, with an exponent $\eta_E = 1.22 \pm 0.08$. In this phase, the total energy of the system consists mostly of the energy contained in the domain walls connecting the elementary defects and the stray fields created by the (anti)vortex cores in which magnetization

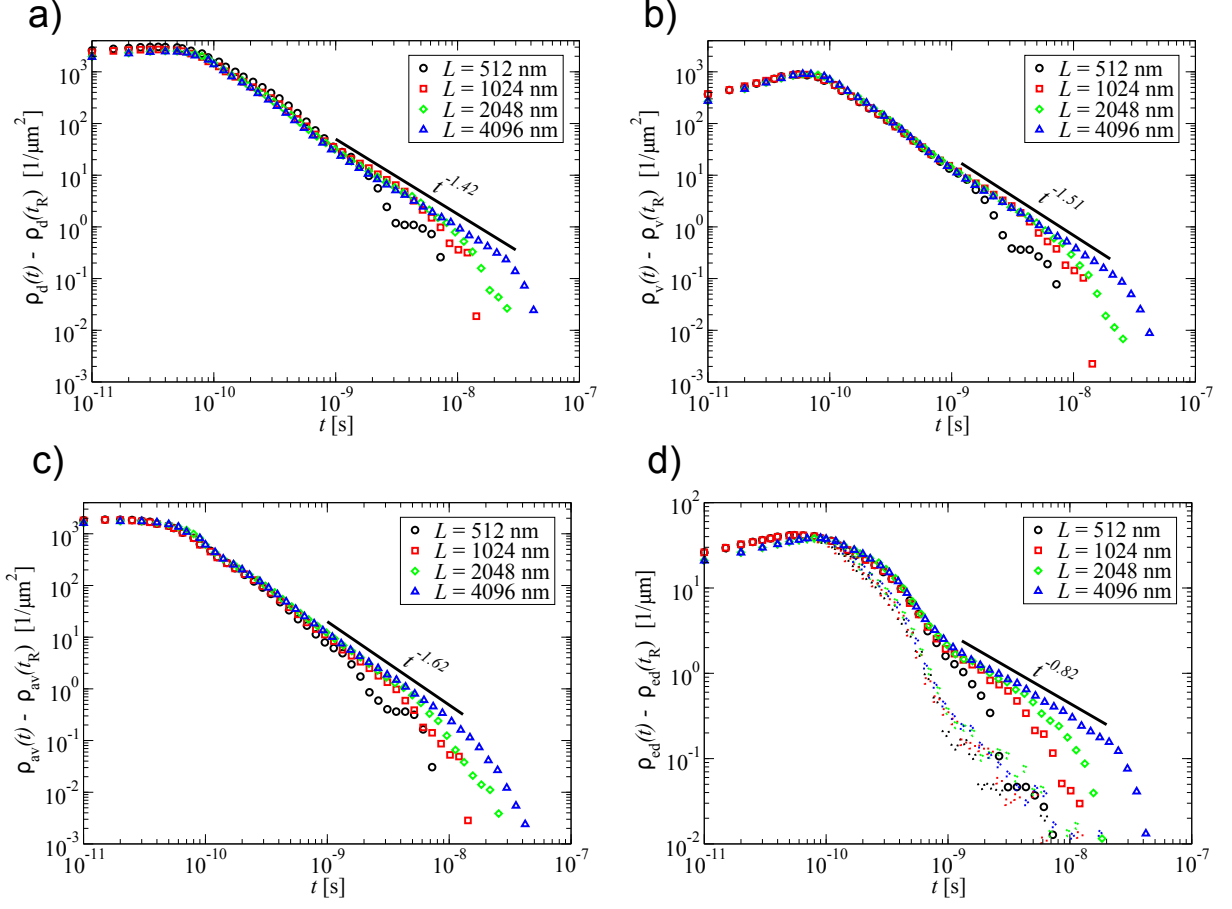


Figure 8. The time evolution of the densities of **a)** all defects, **b)** vortices, **c)** antivortices and **d)** edge defects, with solid lines corresponding to power law fits as guides to the eye. The power laws can be seen most clearly in the largest film sizes. In the case of edge defects, the positive edge defects are noted with dashed symbols.

points out of plane. The largest system sizes are the slowest to reach the energy minimum and thus show the most clear-cut power-law behavior. The inset of Fig. 7 shows that during the coarsening phase the energy density $\rho_E = E/L^2$ of the system is linearly proportional to the density of the defects $\rho_d = N_d/L^2$, where N_d is the total number of all defects. This implies that the defects are the main contributors to the energy at this stage of the relaxation, a result previously obtained for the XY-model by Qian *et al.*¹⁷. The slope changes slightly with system size, likely due to the fact that while the edge defects also contribute to the total energy, their number scales with the lateral film size as $4L$ instead of the L^2 -scaling of bulk defects. Thus the smaller the film, the greater the relative amount of edge defects at the beginning of the simulation. In smaller films the reduction of total number of defects involves more annihilations of edge defects, compared to vortex-antivortex annihilations that dominate in larger films. If the edge defects are energetically less expensive than bulk defects (which would seem reasonable, considering that they don't usually have large out-of-plane components and the overall

change in magnetization direction around the defect is less than that of bulk defects), these annihilations result in smaller decrease in energy than vortex-antivortex annihilations. Hence, for smaller systems, the energy decreases more slowly as a function of the total number of defects.

In the coarsening phase, also the densities of the different defect types decay as power laws, with different exponents for each type of defect. These exponents are determined only by the topological charge of the defect, given that considering separately the chirality and/or core polarization (in the case of vortices and antivortices) did not have an effect on the exponent. The total number density of all defects (counting vortices, antivortices and both types of edge defects) decays as a power law $\rho_d(t) - \rho_d(t_R) \propto t^{-\eta_d}$ with the exponent $\eta_d = 1.42 \pm 0.06$ (Fig. 8 a). Here t_R is again the time after which no annihilations take place. The exponent value is considerably higher than the asymptotic value ($\eta_d = 1$) found in simulations of the XY-model with linear damping and local interactions^{1,17,35}.

For the total amounts of vortices (summing both

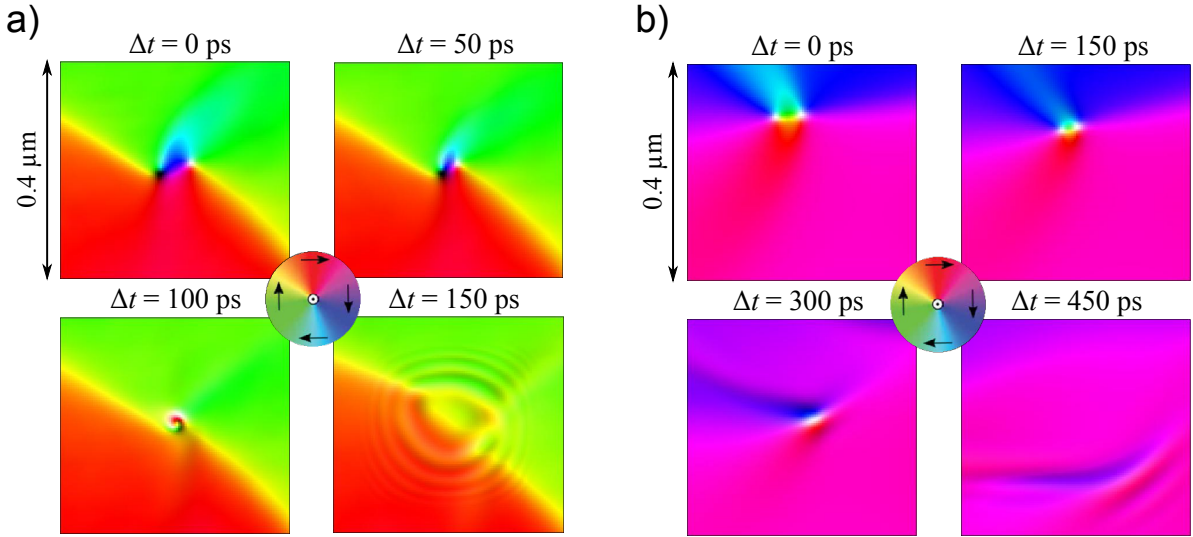


Figure 9. The annihilation of a vortex and an antivortex with **a)** antiparallel **b)** parallel polarizations.

clockwise and counterclockwise rotations and both core polarizations) the time evolution is well-described by a power law $\rho_v(t) - \rho_v(t_R) \propto t^{-\eta_v}$, with $\eta_v = 1.51 \pm 0.05$ (Fig. 8 b). The exponent of the time evolution of the antivortex density ρ_{av} is consistently found to be somewhat larger: We find a power law $\rho_{av}(t) - \rho_{av}(t_R) \propto t^{-\eta_{av}}$ with an exponent $\eta_{av} = 1.62 \pm 0.09$ (Fig. 8 c). Since the typical relaxed state achieved in the simulations is a single-vortex state, $\rho_{av}(t_R)$ is usually 0, though few unrelaxed/metastable end states have $\rho_{av}(t_R)$ between 1-2.

The density of negative edge defects is higher than that of the positive ones in all the simulations. Positive edge defects were observed to be short-lived byproducts of annihilations of vortices and negative edge defects. This supports the notion in Ref.⁹ that negative edge defects are energetically preferable over positive edge defects for films with $Lt > L_{ex}^2$, where L and t are the lateral length and thickness of the film, respectively, and L_{ex} is the exchange length. Like vortices and antivortices, the density of negative edge defects appears to show power-law behavior $\rho_{ned}(t) - \rho_{ned}(t_R) \propto t^{-\eta_{ned}}$, with an exponent $\eta_{ned} = 0.82 \pm 0.09$ (Fig. 8 d). One should note here that for edge defects, $\rho_{ned} = N_{ned}/L$ is a line density instead of an area density. The number density of positive edge defects decays close to zero soon after the initial fluctuations and there's no visible power-law behavior.

B. Defect dynamics during relaxation

Examining the motion of defects during the relaxation/coarsening process reveals complex dynamical defect behavior, including various kinds of annihilations, vortex and antivortex emissions and core switching. All

of these events are restricted by the conservation of the total winding number.

The possible annihilation events are limited to four types: positive and negative edge defect annihilation, vortex-antivortex annihilation, vortex and $2 \times$ negative edge defect annihilation and antivortex and $2 \times$ positive edge defect annihilation. Out of these four annihilation processes, only two were primarily encountered in the simulations: vortex-antivortex annihilation, and vortex and $2 \times$ edge defect annihilation. In the former case, the parallelity or antiparallelity of the polarizations of the annihilating vortex/antivortex pair affects the nature of the annihilation process. This is related to the conservation of another topological quantity, the skyrmion number³⁶.

When the polarizations of the annihilating vortex and antivortex are parallel, the skyrmion number is conserved, resulting in a continuous and relatively slow annihilation process. The vortex and antivortex approach each other until they're indistinguishable and start accelerating in a direction perpendicular to a line connecting them. During the acceleration, the combined vortex-antivortex defect widens and diffuses continuously into the surrounding magnetization. This process is depicted in Fig. 9 a. By contrast, if the polarizations are antiparallel, the skyrmion number is not conserved, and a more abrupt annihilation (referred to as "exchange explosion" by some authors¹⁰) takes place: the vortex and antivortex circle around one another in decaying orbits until meeting at the center and explosively releasing circular spins waves (Fig. 9 b).

The steps of the annihilation process where a vortex annihilates with two negative edge defects are harder to pinpoint. In a typical vortex-edge defect annihilation, one of the edge defects changes sign and emits an antivortex, which annihilates with the approaching vortex. The remaining edge defects, now having opposite signs,

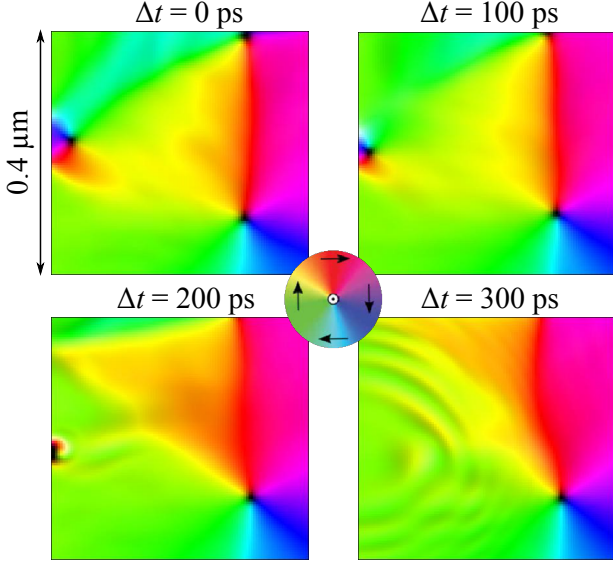


Figure 10. Though somewhat difficult to see, during this edge defect-vortex annihilation, the lower edge defect emits an antivortex with which the vortex actually annihilates.

then annihilate with each other. This kind of annihilation also causes an emission of spin waves (Fig. 10). An edge defect could also absorb or emit a vortex or an antivortex and change sign without a vortex/antivortex close by to annihilate with, since a $+1/2$ edge defect emitting a vortex or absorbing an antivortex and changing into a $-1/2$ defect conserves the winding number. Such emissions and absorptions were observed in the simulations, though in most cases the emitted vortex/antivortex was shortly absorbed again accompanied with an emission of spin waves.

The velocities of the defects do not typically exceed the core switching velocity of Permalloy (340 ± 20 m/s)³⁷. However, sometimes an exception occurs in antiparallel vortex-antivortex annihilations. In this case the increasing velocity of the vortex and/or antivortex causes the formation of a dip particle, an antiparallely polarized magnetization region close to the fast-moving core³⁸. Just before annihilation, the vortex/antivortex exceeds the core switching velocity and the dip particle separates into a vortex-antivortex pair. The consecutive annihilations of the two pairs then take place (Fig. 11). In addition to velocity, the environment of a vortex also affects the possibility of a core switch. Some core switches were observed to happen even for relatively stationary vortices, usually after being excited by a spin wave originating from a nearby annihilation.

Another core switching behavior was sometimes found at the corners of the film: a vortex could "bounce" (shortly get absorbed and then again emitted by the edge defect) between two edge defects on different edges of the film while reversing polarization with each bounce (Fig. 12) and emitting spin waves. This kind of bouncing

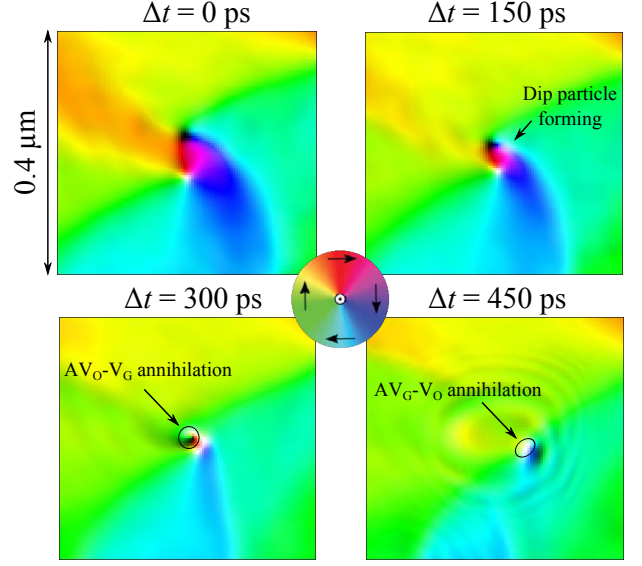


Figure 11. In this antiparallel annihilation, the negatively polarized antivortex (black dot) generates a dip particle which then splits into a positively polarized vortex-antivortex pair. Thus two annihilations occur: an antiparallel annihilation of the original antivortex and the generated vortex (AV_O-V_G), and a parallel annihilation of the generated antivortex and the original vortex (AV_G-V_O).

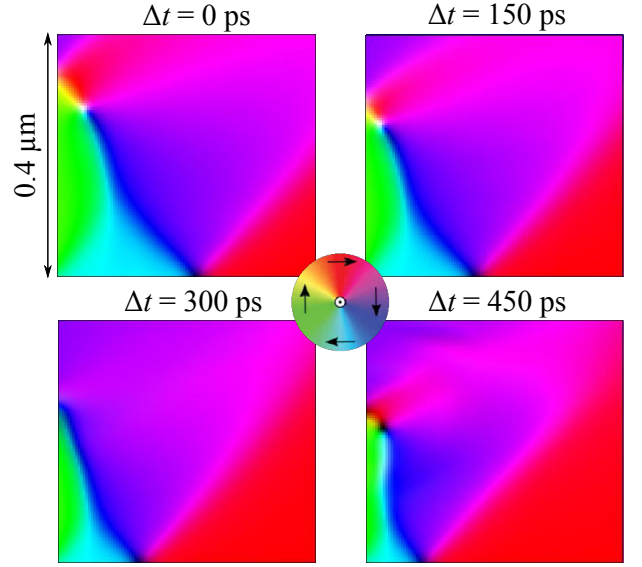


Figure 12. The core switching of a vortex due to a momentary absorption into an edge defect. Usually before and after the absorption and emission of the bouncing defect, the edge defect cores gain short-lived out-of-plane magnetization components.

always ended up in both the vortex and the edge defects annihilating at the corner. Typically there were two or three such core switches before the final annihilation.

C. Effects of damping and quenched disorder

Here, we discuss briefly how the above results are affected by changes in the damping constant α , and when introducing quenched disorder to the system. Fig. 13 shows the time evolution of the total defect density $\rho_d(t)$ in a pure system for different values of α in the range from 0.01 to 0.9; notice that while the higher values of α considered are clearly unphysical for Permalloy, they allow to address the question of how the defect coarsening process is modified when the overdamped limit (as often considered in coarse-grained models of defect coarsening, such as the XY-model) is approached. As indicated by the inset of Fig. 13, the power law exponent η_d evolves from the low- α value of $\eta_d \approx 1.4$ to a lower value of $\eta_d = 1.07 \pm 0.05$ for the highest α -value considered. We note that η_d obtained here in the limit of large α is close to that obtained for XY-model in earlier works^{1,17,35}. The corresponding exponents for the different defect types also exhibit similar evolution with α , with the values obtained for $\alpha = 0.9$ found to be $\eta_v = 1.09 \pm 0.06$, $\eta_{av} = 1.13 \pm 0.06$, $\eta_{ned} = 0.72 \pm 0.09$ for vortices, antivortices and edge defects, respectively (not shown). Qualitatively, with increasing α from 0.01 towards 0.1, the initial fluctuations tend to settle down somewhat faster, and core switching events are found to be less abundant. For the highest α -values considered (0.5 and 0.9), the system forms well-defined defects almost instantaneously, with their subsequent motion being quite sluggish. Also, no core switches nor "bounces" of vortices from edge defects are observed. As a result, the duration of the coarsening phase increases significantly, with the largest system taking more than 70 ns to fully relax in some simulation runs.

Finally, introducing random structural disorder due to the polycrystalline nature of Permalloy to the films with $\alpha = 0.02$ has the effect that some of the simulation runs finish with more than one defect pinned by the disorder. However, for the parameter values used in our simulations for the grain size, exchange coupling reductions across the grain boundary, and saturation magnetization variations in different grains (see Section III), the exponents of the power law relaxations remain the same as in the corresponding pure system (not shown). When the exchange coupling between grains is weakened, the defects prefer to move along the grain boundaries. Additionally, core switches were observed to occasionally occur when a vortex/antivortex crosses over a grain boundary. The probability for such core switches appears to increase with weaker inter-grain exchange coupling strength. Varying the saturation magnetization in the grains makes the movement of the defects somewhat choppy, and increases the chance of defect pinning, but otherwise the dynamics of the relaxation process remains similar to that in the non-disordered Permalloy films considered above.

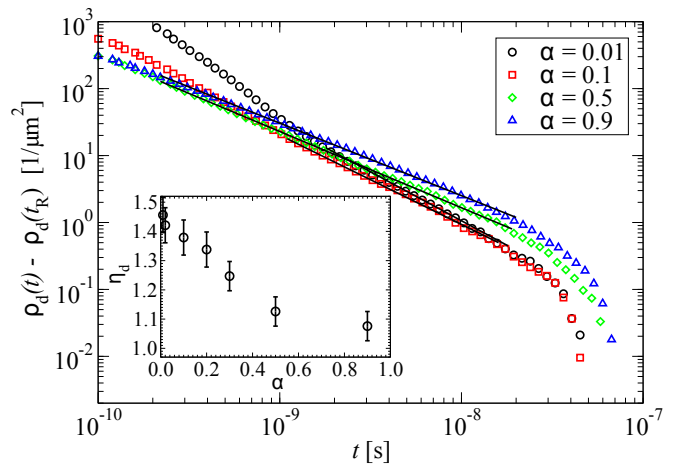


Figure 13. Main figure shows the average time evolution of the total number density of defects ρ_d for $L = 4096$ nm with four different α -values. For larger α , the power law character of the relaxation (black lines indicate the power-law fits used) starts earlier due to the strongly damped initial magnetization fluctuations. The inset shows the resulting η_d -exponent as a function of α .

V. CONCLUSIONS

In this paper, we have investigated the magnetic relaxation starting from disordered initial states of Permalloy thin films of various sizes by extensive micromagnetic simulations. We conclude that the resulting coarsening dynamics involve complex processes and display a multitude of phenomena, such as defect annihilations, core switching and vortex absorption/emission, many of which have previously been individually studied in detail. Together these phenomena result in highly nontrivial dynamics for single defects which then give rise to interesting time evolution of system-wide quantities such as the total energy density and the defect densities.

In the defect coarsening/annihilation phase, this complexity is manifested in particular as slow power-law temporal decay characterized by non-trivial exponents of quantities such as the energy density of the system, of the form of $\rho(t) - \rho(t_R) \propto t^{-\eta_E}$, with $\eta_E = 1.22 \pm 0.08$ for the energy density time evolution. For the defect densities, different values of η were observed depending on the defect type: For vortices, antivortices and negative edge defects we find $\eta_v = 1.51 \pm 0.05$, $\eta_{av} = 1.62 \pm 0.09$ and $\eta_{ned} = 0.82 \pm 0.09$, respectively. The temporal decay of the total density of defects is characterized by the exponent $\eta_d = 1.42 \pm 0.06$. These exponents show little change (within error bars) when using the Gilbert damping constant α within the range of 0.01 - 0.1, and are found to be robust against adding quenched disorder of moderate strength. When α is increased further, the relaxation exponents approach the asymptotic value for the XY-model with local interactions ($\eta_d = 1$)¹. This should be due to the large damping practically eliminating the precessional motion of the magnetic moments so

that they align with the local effective field almost immediately; thus, the dynamics of the magnetic moments starts to resemble that of the XY-model in the no-inertia (overdamped) limit. Our results thus suggest that the relatively low damping of Permalloy has a key role in the emergence of the non-trivial values of the relaxation exponents, and that quenched disorder, present in any real samples, is irrelevant for the relaxation exponent values.

Due to the relatively small size of the films and as a consequence the number of defects (about 500 in the largest films at the initial stages of the coarsening phase), the power-law relaxation phase of energy and defect densities was limited in time to roughly one or two orders of magnitude. Thus, simulations and experiments with larger films and, consequently, longer relaxation times, would be useful. For experimental investigation, time-resolved X-ray imaging techniques should have good enough spatial and temporal resolutions (25 - 30 nm and 70 - 100 ps, respectively)³⁹⁻⁴¹ to observe the defects and

their dynamics. Even though these resolutions are still limited when compared to our simulations, the longer relaxation times and larger inter-defect separations expected during the later stages of the relaxation process in larger films (e.g., with linear sizes in the range of tens of microns) should make it possible to experimentally observe the approximate time evolution of the vortex/antivortex number densities.

ACKNOWLEDGMENTS

We thank Mikko Alava for useful comments. We acknowledge the support of the Academy of Finland via an Academy Research Fellowship (LL, projects no. 268302 and 273474), and the Centres of Excellence Programme (2012-2017, project no. 251748). We acknowledge the computational resources provided by the Aalto University School of Science Science-IT project.

-
- * ilari.rissanen@aalto.fi
- ¹ B. Yurke, A. N. Pargellis, T. Kovacs, and D. A. Huse, *Phys. Rev. E* **47**, 1525 (1993).
 - ² T. Nagaya, H. Hotta, and H. Orihara and Yoshihiro Ishibashi, *J. Phys. Soc. Jpn.* **61**, 3511 (1992).
 - ³ I. Chuang, B. Yurke, A. N. Pargellis, and N. Turok, *Phys. Rev. E* **47**, 3343 (1993).
 - ⁴ C. Harrison, D. Angelescu, M. Trawick, Z. Cheng, D. Huse, P. Chaikin, D. Vega, J. Sebastian, R. Register, and D. Adamson, *Europhys. Lett.* **67**, 800 (2004).
 - ⁵ E. M. Kramer and J. V. Groves, *Phys. Rev. E* **67**, 041914 (2003).
 - ⁶ I. Chuang, R. Durrer, N. Turok, and B. Yurke, *Science* **251**, 1336 (1991).
 - ⁷ R. D. MacPherson and D. J. Srolovitz, *Nature* **446**, 1053 (2007).
 - ⁸ A. J. Bray, *Adv. Phys.* **51**, 481 (2002).
 - ⁹ O. Tchernyshyov and G.-W. Chern, *Phys. Rev. Lett.* **95**, 197204 (2005).
 - ¹⁰ R. Hertel and C. M. Schneider, *Phys. Rev. Lett.* **97**, 177202 (2006).
 - ¹¹ G.-W. Chern, H. Youk, and O. Tchernyshyov, *J. Appl. Phys.* **99** (2006).
 - ¹² L. D. Landau and E. Lifshitz, *Phys. Z. Sowjetunion* **8**, 101 (1935).
 - ¹³ W. Rave and A. Hubert, *IEEE Trans. Magn.* **36**, 3886 (2000).
 - ¹⁴ J. Raabe, C. Quitmann, C. H. Back, F. Nolting, S. Johnson, and C. Buehler, *Phys. Rev. Lett.* **94**, 217204 (2005).
 - ¹⁵ C. Sire and S. N. Majumdar, *Phys. Rev. E* **52**, 244 (1995).
 - ¹⁶ C. Sire and S. N. Majumdar, *Phys. Rev. Lett.* **74**, 4321 (1995).
 - ¹⁷ H. Qian and G. F. Mazenko, *Phys. Rev. E* **68**, 021109 (2003).
 - ¹⁸ V. Estévez and L. Laurson, *Phys. Rev. B* **91**, 054407 (2015).
 - ¹⁹ K. L. Metlov and K. Y. Guslienko, *J. Magn. Magn. Mater.* **242**, 1015 (2002).
 - ²⁰ A. Hubert and R. Schäfer, *Magnetic Domains: The Analysis of Magnetic Microstructures* (Springer Berlin Heidelberg, 2008).
 - ²¹ K. Y. Guslienko, *J. Nanosci. Nanotechnol.* **8**, 2745 (2008).
 - ²² G. S. Abo, Y.-K. Hong, J. Park, J. Lee, W. Lee, and B.-C. Choi, *IEEE Trans. Magn.* **49**, 4937 (2013).
 - ²³ A. Vansteenkiste, J. Leliaert, M. Dvornik, M. Helsen, F. Garcia-Sanchez, and B. Van Waeyenberge, *AIP Adv.* **4**, 107133 (2014).
 - ²⁴ K.-S. Lee and S.-K. Kim, *Appl. Phys. Lett.* **91**, 132511 (2007).
 - ²⁵ C. Luo, Z. Feng, Y. Fu, W. Zhang, P. K. J. Wong, Z. X. Kou, Y. Zhai, H. F. Ding, M. Farle, J. Du, and H. R. Zhai, *Phys. Rev. B* **89**, 184412 (2014).
 - ²⁶ S. Mizukami, T. Kubota, X. Zhang, H. Naganuma, M. Oogane, Y. Ando, and T. Miyazaki, *Jpn. J. Appl. Phys.* **50**, 103003.
 - ²⁷ H. Min, R. D. McMichael, M. J. Donahue, J. Miltat, and M. D. Stiles, *Phys. Rev. Lett.* **104**, 217201 (2010).
 - ²⁸ J. Leliaert, B. Van de Wiele, A. Vansteenkiste, L. Laurson, G. Durin, L. Dupré, and B. Van Waeyenberge, *J. Appl. Phys.* **115**, 17D102 (2014).
 - ²⁹ J. Leliaert, B. Van de Wiele, A. Vansteenkiste, L. Laurson, G. Durin, L. Dupré, and B. Van Waeyenberge, *Phys. Rev. B* **89**, 064419 (2014).
 - ³⁰ J. Leliaert, B. Van de Wiele, A. Vansteenkiste, L. Laurson, G. Durin, L. Dupré, and B. Van Waeyenberge, *J. Appl. Phys.* **115**, 233903 (2014).
 - ³¹ J. Leliaert, B. Van de Wiele, A. Vansteenkiste, L. Laurson, G. Durin, L. Dupré, and B. Van Waeyenberge, *Sci. Rep.* **6** (2016).
 - ³² L. Xu and S. Zhang, *J. Appl. Phys.* **113**, 163911 (2013), <http://dx.doi.org/10.1063/1.4803150>.
 - ³³ V. Baryakhtar, *Zh. Eksp. Teor. Fiz.* **87**, 1501 (1984).
 - ³⁴ O. Chubykalo-Fesenko, U. Nowak, R. W. Chantrell, and D. Garanin, *Phys. Rev. B* **74**, 094436 (2006).
 - ³⁵ H. Toyoki, *Phys. Rev. A* **42**, 911 (1990).
 - ³⁶ O. A. Tretiakov and O. Tchernyshyov, *Phys. Rev. B* **75**, 012408 (2007).
 - ³⁷ S.-K. Kim, Y.-S. Choi, K.-S. Lee, K. Y. Guslienko, and

- D.-E. Jeong, Appl. Phys. Lett. **91**, 082506 (2007).
- ³⁸ R. Hertel, S. Gliga, M. Fähnle, and C. M. Schneider, Phys. Rev. Lett. **98**, 117201 (2007).
- ³⁹ H. Stoll, M. Noske, M. Weigand, K. Richter, B. Krüger, R. M. Reeve, M. Hänze, C. F. Adolff, F. Stein, G. Meier, M. Kläui, and G. Schütz, Front. Phys. **3** (2015).
- ⁴⁰ P. Fischer, M.-Y. Im, S. Kasai, K. Yamada, T. Ono, and A. Thiaville, Phys. Rev. B **83**, 212402 (2011).
- ⁴¹ A. Vansteenkiste, K. W. Chou, M. Weigand, M. Curcic, V. Sackmann, H. Stoll, T. Tyliczszak, G. Woltersdorf, C. H. Back, G. Schutz, and B. Van Waeyenberge, Nat. Phys. **5**, 332 (2009).